Journal of Materials Chemistry A

ROYAL SOCIETY OF CHEMISTRY

PAPER

View Article Online
View Journal | View Issue

Cite this: J. Mater. Chem. A, 2022, 10, 10069

Lithium insertion in hard carbon as observed by ^{7}Li NMR and XRD. The local and mesoscopic order and their relevance for lithium storage and diffusion†

Yuan Fang,[a] Kevin Peuvot,[b] Alice Gratrex,[b] Evgeny V. Morozov,‡[a] Johan Hagberg,§[b] Göran Lindbergh[b] and István Furó*[a]

Received 4th January 2022
Accepted 23rd March 2022

DOI: 10.1039/d2ta00078d

rsc.li/materials-a

We investigate hard carbon fibers in different states of charge by a combination of ^{7}Li-NMR and 2D-XRD. In particular, we record the quadrupole-split ^{7}Li-NMR spectra and ^{7}Li longitudinal relaxation over a wide temperature range, and determine lithium self-diffusion both parallel and perpendicular to the fiber axis. Recording the temperature dependence permits us to interpret the presence of motional averaging of spin couplings for mobile Li. The joint analysis shows that at low Li content, Li occupies sites that lack ordered coordination and delocalized electrons and are collected in disordered spatial domains. Upon increasing the Li content, ordered sites collected in ordered domains become populated. Both disordered and ordered domains have a high inherent heterogeneity with a typical spatial extension of a few nanometers. The disordered domains exhibit a continuous topology that permits unhindered diffusion within it. At high Li content we also observe the presence of very small (∼nm) particles of metallic lithium. The joint analysis of XRD in combination with diffusion anisotropy, and anisotropy from the ^{7}Li-NMR spectrum (with samples oriented differently with regard to the applied magnetic field), shows that the mesoscopic structure is made by ordered domains arranged in a cylindrically rolled-up manner with the mesoscopic axis parallel to the fiber axis.

Introduction

Lithium-ion batteries dominate energy storage for electric portable devices and electric vehicles because their energy density is higher than that of other secondary battery technologies available.[1] A lot of research has focused on further increasing the energy density on the cell level where one motivation is to reduce range anxiety when driving an electric vehicle.[2] Hard carbon has been extensively investigated as a negative electrode material for lithium ion batteries (alongside alternatives such as sodium and potassium ion batteries) since it can provide higher capacity and better cycling performance than the commercial graphite negative electrode.[3–6] It is believed that these advantageous properties are related to a complex heterogeneous structure with more sites suitable for lithium, sodium or potassium storage.[3,7–9]

Various structural models of hard carbon were proposed in the past few decades. The most influential and enduring structural model is that described by Franklin;[10] hard carbon, or non-graphitizing carbon as she named it, consists of nano-scale domains of graphitic carbon held in a random orientation by non-graphitic carbon. The size of graphitic domains was less than 10 nm in the *ab* plane (*i.e.* within a graphene layer), and even less along the *c* axis (*i.e.* normal to the graphene layers), with little or no correlation in the in-layer orientation between adjacent layers. Hence, diffraction studies of such turbostratic carbons give rise to (*hk*0) and (00*l*) peaks, but none of the (*hkl*) peaks observed in crystalline graphite. More recent studies have modified the Franklin model by including curvature.[4,11] With the discovery of fullerene, an sp^2 allotrope of carbon unknown to Franklin, various newer models have proposed that the key to understanding the structure of hard carbon is the presence of non-six-membered rings (*i.e.* pentagons, heptagons, *etc.*), such as the random schwartzite model[12] or the explicit fullerene-like models of Harris,[13] although the concentration of such non-six-membered rings appears to be low.[14] In short, despite more than a century of studies, there is still no model of hard carbon that satisfies and comprehensively explains its physical and chemical characteristics, although it is generally agreed that it is a fairly heterogeneous material in which some regions are more ordered than others.

[a]Division of Applied Physical Chemistry, Department of Chemistry, KTH Royal Institute of Technology, SE-100 44, Stockholm, Sweden. E-mail: furo@kth.se

[b]Division of Applied Electrochemistry, Department of Chemical Engineering, KTH Royal Institute of Technology, SE-100 44, Stockholm, Sweden

† Electronic supplementary information (ESI) available. See DOI: 10.1039/d2ta00078d

‡ Current address: Institute of Chemistry and Chemical Technologies SB RAS, Akademgorodok 50/38, Krasnoyarsk 660036, Russia.

§ Current address: Polarium Energy Solutions AB, Jan Stenbecks Torg 17, SE-164 40 Kista, Sweden.

Besides the microstructure of hard carbon, important aspects of the state and location of lithium within it remain unclear. Regarding the latter, X-ray scattering analysis suggested lithium inserted at two different and broadly-defined sites: in-between graphene sheets (intercalation) and into nano-scale voids,[15–17] where the high voltage slope region in the galvanostatic charge profile was attributed to Li intercalation into graphitic layers and the low voltage plateau region to Li accumulation in nanopores of hard carbon. Contrarily, other evidence suggests the 'adsorption–intercalation' model, where the high voltage part was explained as physical adsorption of Li on graphite surfaces and the plateau part was a result of Li intercalation.[18–20] The actual state of lithium can be sensitively, and in an atomically selective manner, probed by ^{7}Li NMR spectroscopy.[21–25] The primary atomic parameter explored in these studies was the ^{7}Li frequency shift that may vary a lot depending on the chemical environment of lithium. Most importantly, one can typically find that the ^{7}Li spectrum in hard carbon is constituted by several signals in a manner that depends on material properties and preparation. These different signals were interpreted as signatures of Li residing in some distinct environments such as metallic lithium (frequency shift around or above 200 ppm), metallic lithium in nanocavities (50–110 ppm), lithium inserted in graphitic layers (20–45 ppm), and more.[8,9,26–33]

Lithium in hard carbon is quite mobile, making it mandatory to consider the motional averaging effects (as, for example, in Li-containing polymer electrolytes[34]) when interpreting the NMR data. Surprisingly, this was often neglected in past ^{7}Li NMR studies of hard carbon. Moreover, besides the frequency shift, the quadrupole splitting exhibited by the ^{7}Li signals also carries structural information. As we show below, frequency shifts and quadrupole splitting can be jointly interpreted to reveal novel structural features, particularly and consistently so if/when that interpretation is aided by information about lithium mobility furnished by NMR diffusion experiments and information about the (semi-)crystalline and mesoscopic order provided by X-ray diffraction experiments. In this sense, our study points to a more complex yet more informative and consistent experimental approach that can also be applied outside the realm of hard carbons. Conversely, inserting lithium and other metals into carbons and evaluating their NMR scattering features is hereby suggested as another way to evaluate the structure of hard carbons beyond an electrochemical context.

Besides an essential feature required for interpreting our NMR observables, lithium diffusion is also an important property closely related to the charge–discharge processes of batteries.[35–37] Diffusion coefficients have been determined accurately for lithium in graphitic carbon[36] and intercalated graphite LiC_6 and LiC_{12}.[38] There have been attempts to measure lithium diffusion inside hard carbon materials by both electrochemical[18,39,40] and NMR methods,[41] yet further results are needed also because of the variation of the available materials and their relevant properties.

Specifically, here we investigate commercially available PAN-based carbon fibers (CFs) as hard carbon, since they are a suitable and versatile candidate for structural batteries. Structural batteries, where CFs can simultaneously serve as the negative electrode and current collector in LIBs,[42,43] are a new concept that may help lower the overall weight of an electric vehicle and thus increase its range. The insertion mechanism of PAN-based CFs has been previously investigated by following their axial expansion during lithiation[44] and by *in situ* Raman spectroscopy,[45] yet without comprehensively characterizing either the relevant sites in the carbon structure or the lithium state there or the changes in both of these along the different states of charge. What we attempt here is to provide more information regarding these points by combining ^{7}Li NMR spectroscopy including spin-relaxation and diffusion experiments and 2D-XRD. As we are going to show below, the data provide new insights into the distribution and heterogeneity of sites populated in the lithium insertion process. Furthermore, we find that the structural elements containing the graphitic sites exhibit a particular mesoscopic order that corroborates previous microscopic evidence.

Experimental

Sample preparation

The electrochemical insertion of Li into the PAN CFs was carried out in suitable electrochemical cells. In each cell, an approximately 2 cm long bundle of 24 000 PAN CFs (~16 mg) from Toho Tenax (IMS65 unsized) was inserted. The carbon fibers were dried overnight at 60 °C under vacuum prior to cell assembly. Two-electrode pouch cells were prepared in a glove box filled with argon. A copper stripe was used as the current collector for the carbon fibers and a nickel stripe was used for the lithium metal. A 260 μm glass microfiber filter (Whatman, GE Healthcare) was used as a separator and the electrolyte used was 1 M $LiPF_6$ in 1 : 1 wt ethylene carbonate and diethyl carbonate (EC/DEC).

Electrochemical testing

The carbon fibers were galvanostatically cycled with a Biologic VMP-300 potentiostat at a current density of 10 mA g^{-1} between 2 and 0.003 V *vs.* Li/Li$^+$ in a temperature-controlled environment at 25 °C. When the voltage reached 0.003 V *vs.* Li/Li$^+$, the potential was maintained for 5 hours to ensure that the CFs were fully lithiated in the first lithiation. In the second lithiation, the fibers were cycled in the same way as the first cycle but the potential was then maintained for 5 hours in a particular state of charge (0.5 V, 0.3 V, 0.15 V, and 0.003 V *vs.* Li/Li$^+$). These four samples (see Table S1†) were characterized with ^{7}Li NMR spectroscopy. After being cycled, the CFs were washed with DEC (99.9% pure, anhydrous, Sigma Aldrich) and cut into half (1 cm bundle) and gathered into a bigger but shorter bundle in the glovebox filled with argon. The 1 cm long bundle of approx. 48 000 fibers was then placed at the bottom of a 5 mm NMR tube that was sealed to be air and moisture tight.

NMR

^{7}Li NMR spectra at various temperatures were recorded by single-pulse experiments on a Bruker Avance-II 300 MHz

spectrometer at a resonance frequency of 116.6 MHz for ^{7}Li. The typical pulse length of a $\pi/2$ pulse was 4.3 μs for the autotune BBO probe used. The recycle delay was chosen to be long enough (longer than $5T_1$) in relation to the longitudinal relaxation time T_1 (measured by inversion recovery). ^{7}Li NMR spectra were recorded and displayed with aqueous solution of LiCl as the external shift reference for which the ^{7}Li shift was set to 0 ppm.

The specific capacity of the investigated samples is listed in Table S1.† The relative NMR integral of samples loaded with different lithium contents changes roughly linearly with specific capacity. The sole deviation from the linear trend is for the sample with the lowest capacity and the reason is probably that there is still a ^{7}Li NMR signal from the residual electrolyte which overlaps with the low-frequency quadrupolar satellite (see below) of the lithium signal.

Signal loss by the skin effect was tested by recording the ^{7}Li NMR integrals also at 194.4 MHz (on a 500 MHz spectrometer) and the results (see ESI†) indicate no significant radiofrequency (rf) shielding effect from the conductive carbon matrix. This was also verified by estimating the skin depth (see the ESI†) to be approx. 110 μm and 142 μm at 194.4 MHz and 116.6 MHz NMR frequencies, respectively. These values are far larger than the fiber diameter 5 μm, and therefore, we henceforth consider that all lithium ions inserted into PAN fibers are fully detected by NMR.

NMR tests of the temperature stability of the samples and the NMR diffusion experiments

Lithium diffusion in the PAN-based CFs is slow[39] and, at room temperature, it is rendered undetectable by NMR diffusion experiments. Specifically and as also discussed below, the transverse relaxation of ^{7}Li at room temperature is too rapid in this material and therefore one cannot employ sufficiently long gradient pulses. Hence, the diffusion decay at room temperature was insignificant despite the high-gradient probe used and became detectable only at higher temperatures. Increasing the temperature increases the self-diffusion coefficient (and yields more permissive transverse relation times) yet we had to make sure that the samples tolerated higher temperatures for the experimental time (as below, about 8 hours). Hence, the temperature stability of the lithiated samples was tested at temperatures up to 373 K by recording the chemical shift over time (see Table S2†). We found a chemical shift change of less than 1 ppm at 343 K over 24 hours and from that we concluded that the samples are essentially stable at this temperature over the extent of a diffusion experiment (or even several ones). Therefore, we recorded the diffusion data presented here at 343 K. (We note that for a time period of <30 minutes required to record good-quality spectra, the samples can be considered stable even up to approx. 370 K).

The actual NMR diffusion experiments were carried out on a Bruker Avance-III 500 MHz spectrometer (194.40 MHz for ^{7}Li) equipped with a Bruker DIFF60 probe with a 5 mm ^{7}Li rf insertion. The typical pulse length of a $\pi/2$ pulse was 7.8 μs. The diffusion data (see Table S3† and figures below) were produced by a stimulated echo sequence with a longitudinal eddy current delay[46] and the diffusion time Δ and gradient pulse δ set in the ranges 85–200 ms and 0.5–1 ms, respectively, and the gradient strength g increased linearly from 5 to 1350 G cm^{-1} in 12 steps (estimated values of the apparent transverse relaxation time for the central ^{7}Li peak and the longitudinal relaxation time, respectively, that limit the choices of δ and Δ values are listed in Table S4†).

The diffusion experiments were performed with the CFs oriented either parallel or perpendicular to the applied magnetic field gradient. In the first case, it is the diffusional displacement along the fiber axis that is detected and that is essentially unhindered by the macroscopic fiber structure. In the second case, one must consider that the fibers are roughly of $2r = 5$ μm in diameter which may seem comparable to the diffusional displacement during the experiments performed. Whether or not the finite fiber width limits our diffusion displacement (and thereby potentially provides us with coefficients lower than actual diffusion coefficients), it can be established by investigating[47] the parameter $(\Delta D)/r^2$. Its value for our situation (see below) is roughly 0.04 and in this regime the limiting effect of the fiber wall on the diffusional decay is small. Hence, under all circumstances the obtained diffusion coefficients reflect the effect of the carbon material microstructure on the Li diffusion.

X-ray diffraction

XRD patterns from pristine IMS65 fibers, lying flat on the sample stage in Bragg–Brentano geometry, were recorded on a PANalytical X'Pert Pro. The goniometer radius was 240 mm, which was operated in theta–theta mode. The X-ray source was an Empyrean Cu tube (40 mA, 45 kV). The X'Pert Pro was used without a monochromator and with CuKα_{1a} (1.540596 Å); CuKβ radiation was filtered out using a nickel film and the effect of CuKα_{1b}, CuKα_{2a}, and CuKα_{2b} was removed using the 25 bar per weight algorithm developed by Dong *et al.*[94] XRD patterns of ex situ cycled IMS65 fibres were recorded using the P03 microfocus (MiNaXS)[48] beamline at PETRA III, in Debye–Scherrer (transmission) geometry. Cycled fibers were placed into cylindrical quartz capillaries (Hilgenberg GmbH product 4017515, outer diameter:1.5 mm, wall thickness:0.1 mm), which were sealed with Cristaseal (Hawksley & Sons Ltd., purchased through VWR). The incident photon wavelength was 0.968626 Å (12.8 keV). The patterns were recorded on a Pilatus 300K area detector, and processed in DPDAK[49] to correct detector tilt, polarization effects, *etc.* LaB_6 was used to calibrate the sample-to-detector distance.

A measured scattering pattern is the sum of several coherent and incoherent contributions.[50] Information regarding the spatial distribution of atoms is contained in the structural factor $S(q)$, where $q = 4\pi \sin\theta/\lambda$ and several suitable corrections (see the ESI†) are required to extract its true value from the data. One particular correction peculiar to disordered materials such as IMS65 CFs concerns the effect of the observed intensity decreasing with increasing scattering angle. In well-ordered, crystalline materials, this is largely unimportant, since the

Bragg peaks are sharp, and therefore the difference in the angle between the low-angle and high-angle sides of the peak is small. Disordered materials, however, lack true Bragg peaks, presenting instead broad features over a comparatively large angular range. This so-called 'fall-off' makes the high-angle side of features less intense than the low-angle side.

Results and discussion

The main objective of this paper is to derive structural insights from ^{7}Li NMR observations. In particular, we wish to explore the main features of the existing structural models[9,10,12,16,18,19,51,52] that were proposed for hard carbon and investigate whether they are consistent (or not) with the novel data presented here. Irrespective of the actual model, lithium can be assumed to be located in two kinds of domains: one that is more ordered and henceforth identified as the "ordered" domain and the one that is less ordered and thereby called the "disordered" domain. We do not assume that these categories are either absolute or, within themselves, homogeneous – rather, such a model is a rough attempt to capture the essential features of structural variation within the material. In this sense, what we simply state is that irrespective of the actual distribution of structural features, we try to rationalize some observations below in a two-state model where the "ordered" state is the integral representation of those regions/sites available for lithium that are graphitic and the "disordered" state is, basically, the rest of the material where a crystalline-like order is less present or absent altogether. As we are also going to explicitly show below, this two-state model is a gross over-simplification (yet, at the same time, useful). We are also aware that many structural models had more specific sites proposed, yet feel that many such proposals lacked an unequivocal verification. Finally, the samples we investigate lack significant metallic domains as we tried to remain in the electrochemical regime most relevant for battery operation and, hence, outside significant electrochemical deposition of metallic lithium, so-called lithium plating.

Electrochemical performance

A typical galvanostatic profile of the carbon fibers explored here is shown in Fig. 1. The specific capacity (that is, the formal Li content) decreases by 20% between the first lithiation (384 mA h g^{-1}, corresponding to $LiC_{5.8}$) and the first delithiation (307 mA h g^{-1}). The surface area of the PAN fibers is 0.42 m^2 g^{-1}, *i.e.* one order of magnitude lower than the surface area of a graphite electrode which has a specific surface area of ~5 m^2 g^{-1}.[53] This difference in the surface area is also observed at the same ratio when looking at the double layer capacitance as showed in another study.[42] As the surface area of the PAN fibres is low, the irreversible capacity loss can be mainly attributed to trapped ions in the PAN fibre microstructure and less to surface electrolyte interface (SEI) layer formation.[53] In hard carbon electrodes, the typical galvanostatic profile is constituted of more distinguishable steps/stages with a slope at higher potentials and a plateau at lower potentials.[27,29,31,54,55] Contrary to other hard carbon electrodes, we observe no extensive plateau at low voltages that possibly indicates heterogeneity in the insertion mechanism. Indeed, we explore this latter notion below. Samples with different states of charge as indicated in Fig. 1 were used for NMR and XRD and are defined in Table S1.†

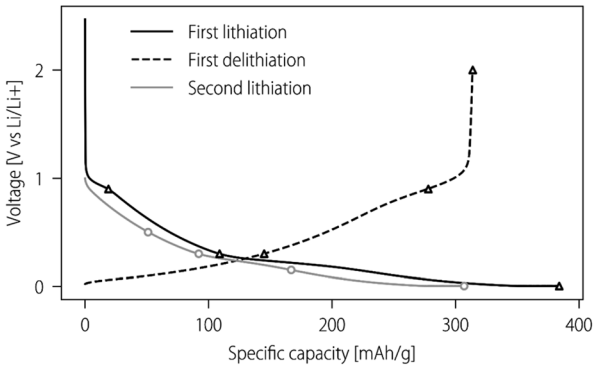

Fig. 1 Galvanostatic profile of the IMS65 unsized carbon fibers cycled at 10 mA g^{-1} followed by a potentiostatic step for 5 hours. The four NMR samples with different lithiation degrees studied here are indicated as circles in the 2nd cycle. Similarly, the six triangles in the 1st cycle indicate samples used in XRD studies.

Motional averaging of NMR spectral parameters and the spatial extension of the relevant structural features

In Fig. 2 and 3, we present two essential features that set up the starting point for our considerations. Fig. 2 presents the lithium self-diffusion coefficients, measured by ^{7}Li NMR diffusion experiments at 343 K, that vary between 1.4×10^{-11} m^2 s^{-1} for the fully lithiated sample and 5.9×10^{-13} m^2 s^{-1} for the sample with the lowest Li content. Fig. 3 shows the NMR spectra for the samples at different degrees of lithiation at high temperature. ^{7}Li is an $I = 3/2$ nucleus, and although it has a rather small nuclear quadrupole moment Q, it can exhibit a quadrupole-split

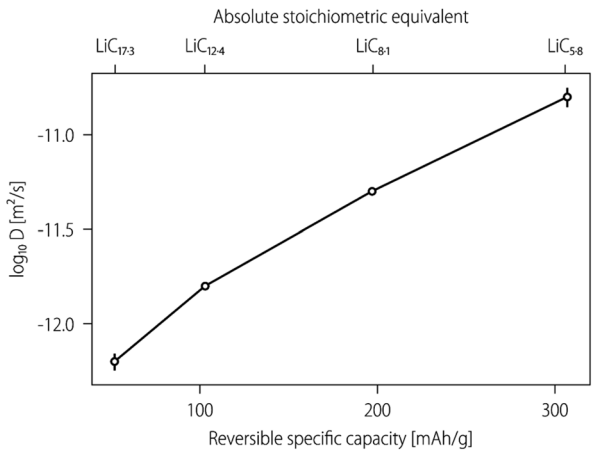

Fig. 2 Self-diffusion coefficients of ^{7}Li in samples with different lithium contents, recorded at 343 K and in the direction parallel to the fiber axis. The reversible specific capacity is indicated along the lower x-axis, and the absolute stoichiometric values of the individual samples are indicated above.

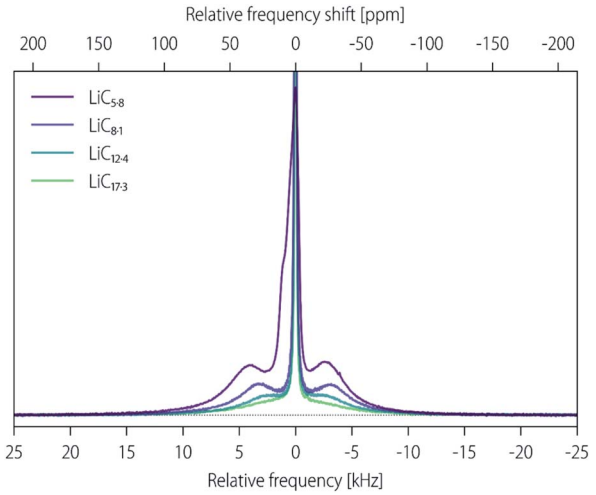

Fig. 3 Comparison of line shapes of lithiated PAN fibers with different lithium contents at 353 K. The main peak positions were aligned so that the behavior of quadrupole satellites can be better compared visually and the vertical axis is truncated to focus on the satellites. Spectra at other temperatures are shown in Fig. 5 and S1.†

NMR spectrum. Such spectra consist of a central peak containing 40% of the spectral intensity and two symmetrically placed (at frequencies $\pm\, \nu_Q$ relative to the central peak) satellite manifolds that jointly contain 60% of the spectral intensity.

The placement (and width) of the satellites depends on the quadruple coupling strength that in turn depends on the electric field gradient (efg) tensor V set by local atomic coordination at the site of the ^{7}Li nucleus. In the simplest and frequent case of an efg tensor of zero asymmetry factor (in systems with higher than threefold symmetry, such as LiC_6), the quadrupole frequency shift of the satellite away from the central line is given as[56]

$$\nu_Q = \frac{e^2qQ}{4\ h}\left(3\cos^2\theta - 1\right) = \chi_Q\left(3\cos^2\theta - 1\right) \qquad (1)$$

where $eq = V_{zz}$ is the largest element of the efg tensor V_{ij} along its principal axis z, e is the elementary charge unit and θ is the angle between the principal axis and the applied magnetic field. In an oriented sample, such as single crystals, with a single value of θ and a single value of eq, the satellites arising from different parts of the sample contribute at the same frequency and the result is, typically, narrow satellite peaks. If these conditions are not met (as in powdered samples, *i.e.* local environments oriented differently with regard to the external magnetic field, or inhomogeneous samples with atomic environments varying with regard to coordination), the satellite peaks are broadened.[57] In a random powder where the $\theta = 90^\circ$ orientation is more frequent than the $\theta = 0^\circ$ orientation, the resulting spectral form is a typical "powder pattern".[58] One condition for quadrupole splitting is a suitable environment with not too high symmetry. In Li metal (bcc) for example, the coordination is cubic and the efg vanishes while the efg is nonzero in LiC_6 in which the principal axis is the surface normal to the graphite planes. The efg should not vanish in a turbostratic system (that is, with rotationally random stacking of graphene sheets). It is probably fair to say that little is known for certain about the instantaneous local value of efg, except the ordered phases of metallic Li and LiC_6.

Yet, lithium in carbon is a mobile species and thereby its environment is not defined by any instantaneous atomic coordination and/or local orientation but by the *average* of that over the sites that are diffusionally sampled by lithium over the time scale relevant for the actual experiment.[57] In the case of recording simple spectra (as shown in Fig. 3), the relevant time scale is $\tau \sim 1/\nu_Q$ where ν_Q is the instantaneous value of the quadrupole splitting set by the local atomic coordination as shown in eqn (1). We assume that the characteristic value of ν_Q can be estimated as $\nu_Q \approx 11.5$ kHz observed[26–28] in LiC_6 from which we can conclude that the relevant time scale for motional averaging is roughly 100 μs. Over the time and with the average diffusion coefficient as shown in Fig. 2 for the high-Li-content sample, the average diffusional displacement becomes $(6D\tau)^{1/2} \sim 50$ nm at 343 K (and ~15 nm for the low-Li-content sample). This length scale is much larger than the size of the intermingled structurally distinct regions (a few nanometers) that were observed by, *e.g.* electron microscopy in the type of hard carbon investigated here.[45,59]

Hence, at higher temperatures we can expect NMR spectra that essentially reflect the average properties of the sample studied over mesoscopic (in the order of 10^1–10^2 nm) length scales. Here, the quadrupole splitting as revealed by the spectrum is the average both with regard to the distribution of the efg magnitude and orientation within the motionally averaged volume, and among other things, the result depends on how the local orientations are distributed. If the distribution within the explored volume is isotropic, $\langle 3\cos^2\theta - 1\rangle$ becomes zero and no quadrupole splitting is detectable (this can be the case for Li in an amorphous environment with no long-range order). If the material has some anisotropy expressed by a local (that is, within the motionally averaged volume) director, it will replace the principal axis in defining the orientational dependence. Conventionally,[60–62] the effect of this averaging is expressed as

$$\nu_Q^{\text{average}} = \langle\chi_Q\rangle(3\cos^2\theta_{\text{dir}} - 1) \qquad (2)$$

where θ_{dir} is the angle between the applied magnetic field and director for the motionally averaged region and $\langle\chi_Q\rangle$ is the residual quadrupole coupling constant averaged both over the variation of the efg strength and its orientation relative to the local director.

Besides the quadrupole coupling being anisotropic, the frequency shift (also see below, the Knight shift arising from the paramagnetism of free electrons in systems containing such cases or chemical shift arising from the diamagnetic response of electrons localized in covalent bonds) is also an inherently anisotropic property and varies over sites according to the variation of the local electronic structure. Regarding anisotropy, the anisotropy of the ^{7}Li Knight shift in LiC_6, as expressed by the difference between shift values obtained with the magnetic field parallel and perpendicular to the c axis, is roughly 16 ppm (ref. 63) that, in the field where we recorded our spectra, yields

a frequency difference of roughly 2 kHz between different orientations. This value is much smaller than the corresponding difference in quadrupole coupling constants. Any local susceptibility effect (caused by material inhomogeneity/anisotropy) is in a similar order. Hence, processes that lead to a motional averaging of the quadrupole coupling should lead to a similar (or, spatially, even larger) extent of averaging of the frequency shift (plus macroscopic susceptibility) variation. On the other hand, if metallic lithium (with its Knight shift over 200 ppm) is present, the shift variation between different possible environments becomes one order of magnitude larger and thereby comparable, on the frequency scale, to that of the quadrupole coupling. Hence, there is no complete motional averaging if the samples prepared contain suitably large metallic domains.[64]

As discussed above, the instantaneous coupling fluctuates not only because of the spatial motional averaging but also because of any local motions at the local coordination sites. The effect of this is spin relaxation. In particular, longitudinal spin relaxation presented in Fig. 4 is sensitive to the high-frequency (comparable to the inverse of the Larmor frequency) part of the power spectrum with the fluctuations (spectrum density function). Since quadrupole coupling is typically larger than other spin couplings and it is a property that is more local (thereby modulated at higher frequencies by translational motion) than the frequency shift, one can plausibly expect that the observed relaxation is dominantly quadrupolar.

As is detailed in the Experimental section, the self-diffusion coefficients could only be measured at rather high temperatures. Hence, we do not know what the relevant values at low temperatures were. On the other hand, the longitudinal spin relaxation rate $R_1 = 1/T_1$ could be readily estimated in a wider temperature range (see Fig. 4). The observed linear variation on the logarithmic scale indicates that the slope of the R_1 values reflects the temperature variation of the correlation times that are connected to the motional modulation of the quadruple coupling of the ^{7}Li nuclei. Self-diffusion is the longer-scale consequence of the motional spectrum. Hence, with an activation energy of roughly 10 kJ mol^{-1} that can be inferred for a high-Li-content sample from the data shown in Fig. 4, we can estimate that at 135 K (see below) the diffusion coefficient decreases 200-fold and the average diffusional displacement becomes $(6D\tau)^{1/2} \sim 3.5$ nm for the high-Li-content sample.[65] That is, indeed, in the same order as the size of the structural features visualized by other methods. For a low-Li-content sample, the activation energy is slightly higher and the diffusion coefficient at 343 K is lower and thereby the diffusional displacement becomes $(6D\tau)^{1/2} < 1$ nm.

On the other hand, spin relaxation is influenced also by local fluctuations that do not lead to translational displacement. Therefore, the activation energy inferred from spin relaxation as shown in Fig. 4 is often significantly lower (though never higher)[66–74] than that inferred from the temperature dependence of the self-diffusion coefficient or ionic conductivity. For LiC_6, the difference between these two activation energies was roughly a factor of 2.[65] If the same relation was also valid for the hard carbon material here, then the diffusion coefficient in the high-Li-content sample would be shown to decrease 4×10^4-fold at 135 K relative to that at 343 K and the diffusional displacement $(6D\tau)^{1/2}$ would decrease to a few tenths of a nanometer. Hence, we can conclude that at 135 K the local atomic heterogeneity within the sample is imprinted in the spectra. In general, previous studies aimed at analyzing ^{7}Li NMR spectra in terms of the structure often did not consider the time and length scales and their spectral relevance sufficiently well as discussed above.

The temperature dependence of the ^{7}Li NMR spectra: carbon environments

The ^{7}Li NMR spectra of the fully lithiated PAN carbon fibers in the 373 K to 135 K range are presented in Fig. 5a. At higher temperatures, we can observe a central line and quadrupolar satellites whose position yields $\nu_Q^{\text{average}} \approx 3$ kHz quadrupole splitting. The frequency shift that is presumably a combination

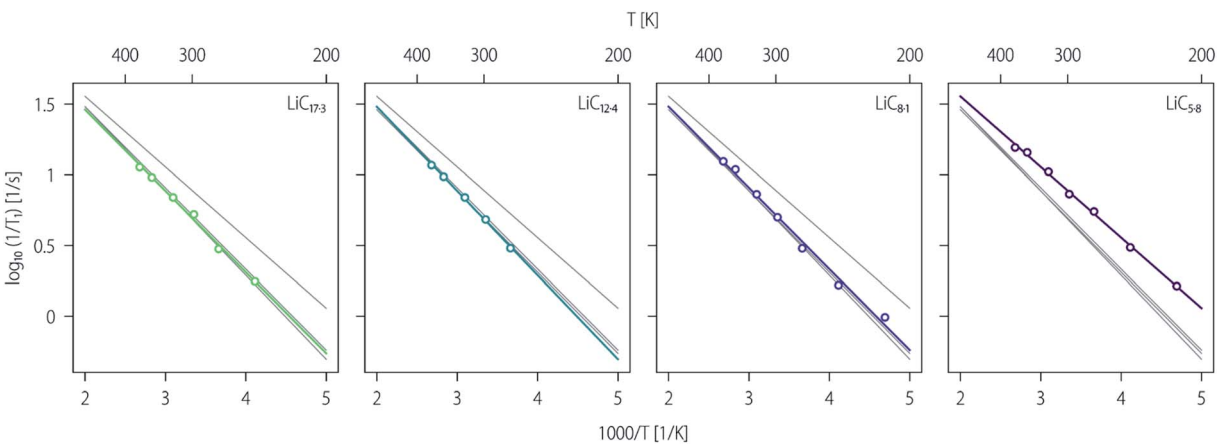

Fig. 4 The temperature dependence of the longitudinal relaxation rates (in s^{-1} units). The slopes provide an estimate of approx. 10 kJ mol^{-1} for the activation energy of the correlation time for motions that modulate the quadrupole coupling of ^{7}Li nuclei. For ease of comparison between similar curves, each sample investigated is shown in its own subplot with circles and a coloured line, and all other samples with a thin grey line.

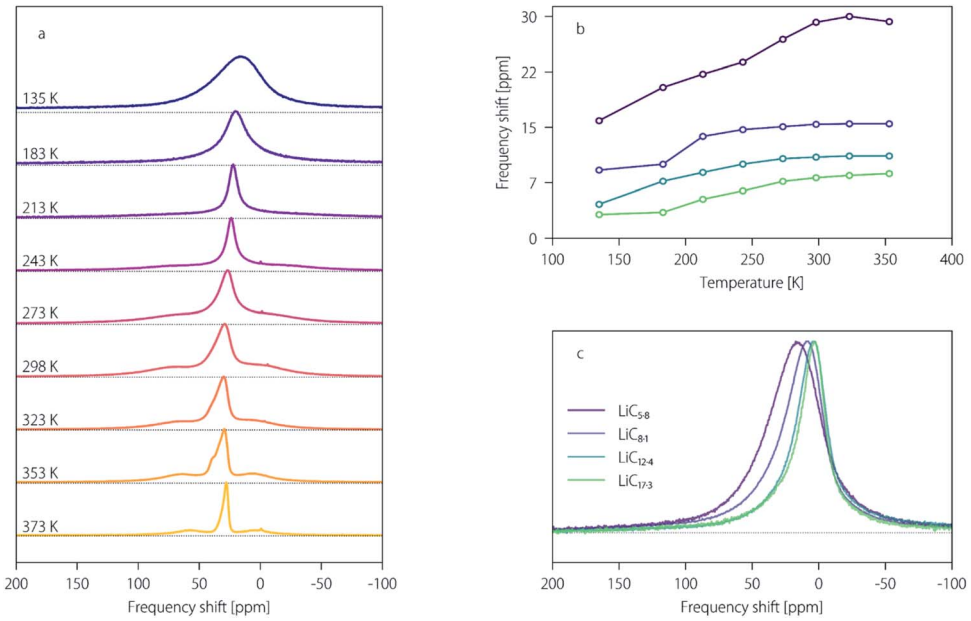

Fig. 5 (a) ^{7}Li NMR spectra of fully lithiated PAN carbon fibers ($LiC_{5.8}$) at different temperatures, (b) the total frequency shift containing both paramagnetic (Knight shift) and diamagnetic (chemical shift) effects as estimated from the position of the main ^{7}Li peak, (c) the spectra recorded at 135 K for samples at different degrees of lithiation. In (a and c), the maximum spectral amplitudes were set to identical values.

of chemical shift (arising from electrons localized over atoms and bonds) and Knight shift (paramagnetic effect arising from free electrons), is roughly 30 ppm at room temperature, a value similar to that (27 ppm) reported for the fully lithiated phase of the turbostratic structure in mesocarbon.[26] Yet, the central peak shape clearly indicates that there is a sizeable shift distribution contributing to the spectral shape (namely, the shoulder visible in the 353 K spectrum shown in Fig. 5a has a shape that is quite typical for residual shift anisotropy) and thereby small differences between shift estimates should be handled with caution. The variation of the estimated shift with temperature is shown in Fig. 5b.

The main trend observed with decreasing temperature is the same as that observed, though in less detail, before the spectrum broadens.[27] In addition, the quadrupolar satellites seemingly vanish here. These observations are a consequence of structural heterogeneity below the mesoscopic length scale that affects the spectrum once suitable motional averaging ceases. On the one hand, the local quadrupole splitting ν_Q varies over sites, depending on the local coordination, between, presumably, 11.5 kHz (the LiC_6 value) and zero. Spreading out satellite spectral intensity in such a broad frequency range makes its spectral contribution disappear into the spectral baseline. At higher temperatures, all the spectral intensity becomes collected around the average splitting defined by $\langle\chi_Q\rangle$, thereby providing resolved satellites.

One particular point to observe is that at high temperatures (353–373 K) the spectrum is rather fully averaged in the sense that besides large-scale orientation effects to which we return below, it reflects the average Li environment. In contrast, the 135 K spectrum reflects the distribution of the *local* atomic coordination and electronic structures. However, at room temperature, partial averaging renders the spectral features singularly uninformative about either average or local properties. Of course, conditions such as the size of structural units may vary from one hard carbon to another, but it is nevertheless such that conclusions drawn from spectra recorded at a single temperature (typically, close to room temperature) are particularly prone to misinterpretation (for example, the shoulder visible at 353 K shown in Fig. 5a could be mistakenly identified as a consequence of two chemical environments).

The frequency shift influences the central line and the satellites in the same manner but for the satellites, its effect is masked by the quadrupolar effects. The central peak broadens considerably to a width of >50 ppm at 135 K thereby reflecting the distribution of the local instantaneous value of the frequency shift. This shows that there is a very considerable variation with regard to the presence of the free (delocalized) electron density. There is a small yet clear presence of spectral intensity at 80–100 ppm frequency shift (see Fig. 5c), which is indicative of some clusters of "quasi-metallic" lithium (possibly located in the closed pores of the hard carbon electrodes).[27,29,31,55] One should note that such "quasi-metallic" Li is usually formed when there is a plateau in the charge–discharge curve at a potential below 0.1 V *vs.* Li/Li^+.[29,31,55] Such a plateau was not observed (see Fig. 1) which supports the molar fraction of these lithium clusters being low. The most probable form of "quasi-metallic" lithium is very small (∼nm) metallic clusters. As has been established long ago, the Knight shift (electron paramagnetism) in such small clusters is reduced significantly, relative to that in bulk metal, and in an apparently monotonic size-dependent manner, relative to that in bulk metal;[75–79] it seems that this feature has seldom been recognized in the context of Li metal deposition in carbon materials.

Nevertheless, the concentration of such species (as revealed by the spectral intensities shown in Fig. 5c) is clearly quite low.

Because of the low content of metallic lithium and because of the relatively low value of the Knight shift for LiC_6-like species, the average shift does not vary as would be expected for a purely metallic species.[80] The temperature trends for the average shifts is shown in Fig. 5b; clearly, the change is the largest for the fully lithiated sample. This is further corroborated in Fig. 5c, where upon increasing the Li content, spectral intensity clearly gets added to the high-shift side. These observations clearly indicate that there are less quasi-metallic and LiC_6-like sites at lower capacities. This is the first indication that at low capacities, the intercalation sites are *not graphitic* and the electronic structure lacks free (delocalized) electrons, supporting the recently developed 'adsorption-intercalation' model, where Li storage in a high potential slope region was attributed to Li adsorption onto the surface and defects and in the plateau region at low potential represents Li intercalation in graphitic layers.[9,18,19]

This conclusion regarding the nature of the intercalation sites at low and high capacities is strengthened by using the high-temperature spectra shown in Fig. 3. At a low Li-content, the average quadrupole splitting is small (in fact, we lack detectable splitting, though the satellite contribution is separable for the central line in the spectrum), thereby reflecting a disordered location where the size/orientation of the local atomic coordination lacks a longer-range order. Expressed in another way, the lack of such an order leads to an effective averaging of the quadrupole coupling even by very small displacement. As is clear, at high Li content there is a significant average quadrupole splitting that is consistent with the fraction of Li residing in small (<10 nm, see the earlier discussion about motional averaging) graphitic structures with suitable anisotropy.

Jointly, the spectral data as discussed above suggest that (i) at low Li content it is the region with no free electrons and no discernible translational order that is intercalated first by lithium while (ii) upon further charging, the lithium sites that are more conductive and more ordered start to be filled. Both of these regions are constituted by small domains, in the order of a few nanometers, that are well intermixed (that is, diffusing lithium can sample them well at high lithiation). Since the fraction of lithium that is in the form of nm-sized metallic particles is small and the stoichiometry at our highest Li content is roughly LiC_6, the lithium atoms seem to sample the carbon structure well (that is, provide structural information that is not biased a lot towards particular carbon environments).

As a final note in this section, there are several previous studies where the ^{7}Li NMR spectra were recorded in a wide temperature range.[27,29,31,55] In most of these cases, the studies focused on the central line behavior and ignored the parallel evolution of the quadrupolar splitting (that is, if any satellites were detected). In all these latter cases, the decreasing range of diffusional averaging was detected as a bifurcation of spectral intensity into peaks with distinct frequency shifts, one of which was typically a distinct and often large bulk metallic peak that indicated large metallic domains (also intentionally created[64]) consistent with lithium being electrochemically deposited on carbon. Finer details of the behavior of the non-metallic peak(s) were seldom analyzed. These features and the sufficiently large difference between the materials investigated here and elsewhere preclude thereby direct and detailed comparisons with most of the work done previously. Conclusions for the distribution of Li over disordered and more ordered regions were, indeed, drawn but we cannot recall any analysis including comprehensive discussion of diffusional averaging.

Structure analysis by XRD

A 2D-XRD pattern typical of IMS65 fibers is shown in Fig. 6a. It is immediately apparent that the pattern is highly asymmetric, with most features preferentially situated along the perpendicular orientation (the fibers are oriented along the '*y*' axis). This is illustrated in Fig. 6b, where the perpendicular orientation has strong small-angle contribution (from porous regions) and broad reflection in the region of 1.75 $Å^{-1}$, which corresponds to the (002) reflection in graphite, expected at 1.87 $Å^{-1}$.[81] Since this reflection is far too diffuse to be considered a true Bragg peak, we here adopt the convention that such broad reflections are analogues of Bragg peaks in a corresponding crystalline structure. In the parallel orientation, no (002) analogue is present (the residual hump in the same region is solely caused by the quartz capillary), but there is instead an analogue of the (100) graphite reflection. This pronounced orientation allows us to neatly combine background subtraction (*i.e.* removal of the signal from the capillary, *etc.*) with removal of Compton and self-scattering (see the ESI†) by simply subtracting the parallel integration from the perpendicular orientation. This also avoids any complications arising from variations in the lithium content (which would have its own Compton/self-scattering contribution), number of illuminated fibers, *etc.*

An example of such a subtraction, after division by using the de-broadening function and correction for the structural factor fall-off, is shown in Fig. 6c. The (002) analogue has a clear asymmetry of its own, with a rise in intensity on the low-q side. This may result from the small number of contributing layers in the turbostratic structure, as described by Warren.[82,83] Since complex models face the risk of overfitting,[84] we adopt a simpler approach in which the (002) analogue is the sum of two distinct Gaussian distributions. In pristine IMS65 fibers, one distribution, $(002)\lambda$, is centered at 1.79 $Å^{-1}$ and has a half width at a half maximum (HWHM) of 0.14 $Å^{-1}$. The other, $(002)\gamma$, is centered at 1.68 $Å^{-1}$ and has a HWHM of 0.33 $Å^{-1}$. In this model, $(002)\lambda$ describes more ordered regions of carbon, since the HWHM is narrower and the interlayer spacing is closer to that of crystalline graphite (1.87 $Å^{-1}$), and $(002)\gamma$ describes the more disordered regions. As is shown in Fig. 6d, the two distributions respond differently to (de)lithiation. During the first lithiation cycle, the $(002)\gamma$ feature responds to very high potentials at the working electrode; at 19 mA h g^{-1} (LiC_{117}), $(002)\gamma$ has already shifted from an interlayer spacing of 3.73 Å to 3.78 Å – a 1.4% increase. In contrast, $(002)\lambda$ has scarcely shifted (3.51 Å to 3.52 Å). This suggests that, at low levels of lithiation, lithium is preferentially inserted into more disordered regions.

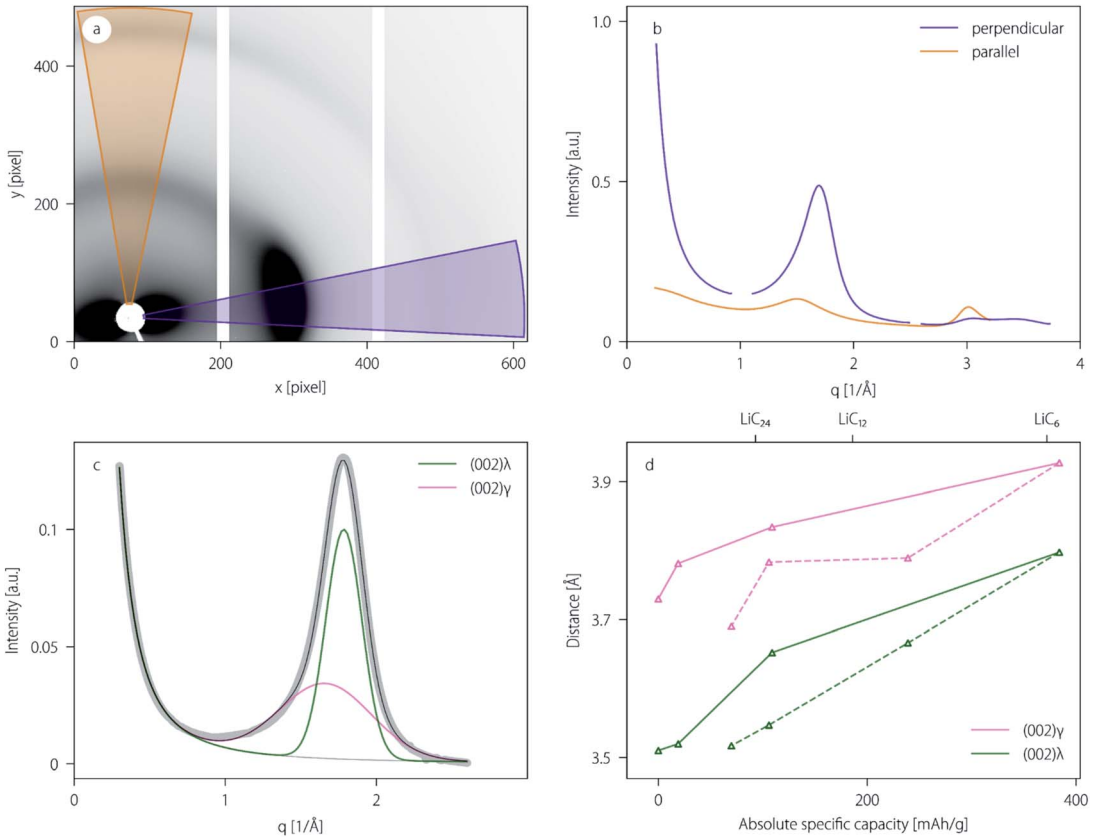

Fig. 6 (a) A typical 2D X-ray pattern from cycled IMS65 fibres, (b) naïve integrations of the perpendicular and parallel orientations, (c) deconvolution of a corrected perpendicular orientation, (d) the response of the two distributions within the (002) analogue to (de)lithiation.

Both the ordered (002)λ and disordered (002)γ display obvious hysteresis loops in the first (dis)charge cycle. The overall change in the interlayer spacing is more dramatic for (002)λ than for (002)γ, but, given its lower initial value, this is unsurprising. It is interesting to note, however, that the fully delithiated sample (LiC_{29}) has a lower final value for (002)γ than the pristine sample (3.69 Å and 3.72 Å respectively). This suggests that lithiation has annealed the disordered regions, providing enough energy for the carbon sheets to reach a more graphitic structure than they initially had.

Li dynamics in carbon environments and its relevance for local and mesoscopic structures

After having established our structural model, we turn our attention back to dynamic features shown in Fig. 2 and 4. Fig. 4 in particular shows that the activation energies for local (that is, at the coordination sites) motions at low and high Li contents are essentially the same. This activation energy is, however, at least a factor of 2 lower than the corresponding activation energy in crystalline LiC_6.[65] Since, in particular, our activation energies at high (both ordered and disordered domains are filled) and low (only the disordered domains are filled) Li contents are close, this also means that the activation energy in our ordered domains is at least a factor 2 lower than that in LiC_6. Hence, our ordered domains are only relatively (that is, in comparison to the disordered domains) "ordered" but are much more defective than crystalline LiC_6. This is in line with the large width of the XRD reflections discussed above.

While local motions are perhaps similar in the disordered and ordered domains, the translational diffusion is clearly different in them. As direct evidence, we have provided the data in Fig. 7 where we have displayed the diffusion coefficients obtained in the direction parallel and perpendicular to the fiber axis. The experimental values (not their logarithms as in the figures) are shown in Table S3† and illustrative diffusional decay in Fig. S2.† At the lowest Li content, it is only the disordered regions that contain Li and in this situation the diffusion coefficients in the two directions are close to each other. This, first of all, strengthens further the notion that the disordered regions indeed lack a longer-range order. The ordered regions are not filled and, concerning Li motion, they provide barriers that hinder diffusion by excluding pathways through their volume. In particular, the ordered regions are more graphitic and such structures are often conceptualized and pictured as flattened flakes (as also shown in Fig. 7). Flat objects hinder diffusion much more effectively in the direction of their short axis.[85,86] Hence, with flattened graphitic flakes we would expect the diffusion coefficient perpendicular to the fiber axis to be lower than that parallel to the fiber axis. This is clearly not the case and this suggests that the graphitic regions are not of significantly different extensions along their c axis and perpendicular to their c axis.

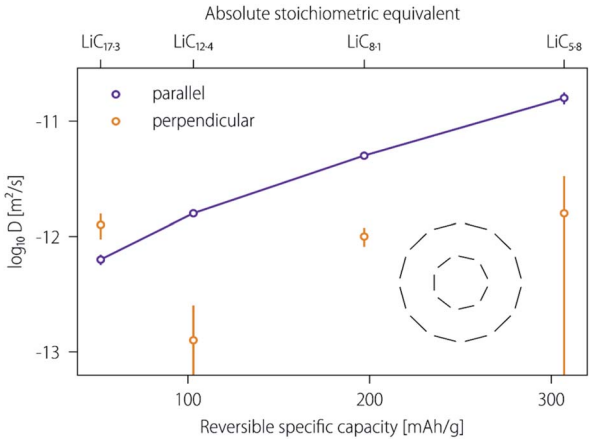

Fig. 7 Translational self-diffusion coefficients measured in directions parallel and perpendicular to the fiber axis at different Li contents. Note that for the $LiC_{12.4}$ and $LiC_{5.8}$ samples the error is comparable to the actual value, as shown in Table S3,† and the error bars are cut because of the logarithmic scale. The inset shows the proposed cross-sectional mesoscopic texture within the carbon fibers with a rolled-up structure of the ordered domains schematically indicated by the bars representing the directions of the graphitic layers as seen from the direction of the fiber axis.

Upon increasing the Li content, the diffusion coefficient along the fiber axis increases significantly while that perpendicular to the fiber axis remains roughly the same. The faster diffusivity of Li parallel to the graphene plane than perpendicular was reported for graphite[36] and basal graphene layers.[37] Moreover, the transverse electrical resistivity of a single carbon fiber was found six times greater than the longitudinal resistivity,[87] in agreement with our result here. There are at least three possible mechanisms that we have to consider as contributing factors. First, upon Li loading the fiber expands as a consequence of the microscopic expansion of the carbon matrix. Secondly, as the ordered domains start to be filled (as shown in in Fig. 3 the small but discernible quadrupolar satellites for the 0.30 V sample) they do not provide an impermeable hindrance for Li diffusion any more. Finally, one can plausibly expect that diffusion in the ordered regions perpendicular to the *c* axis (similar to LiC_6) is much faster.[65]

The expansion of the carbon matrix seems to have no significant effect in defining our observations. First of all, the local motions remain largely unaffected (recall Fig. 4). Secondly, at least in the disordered region the matrix expansion should influence diffusion in all directions while the experimental diffusion coefficient only increases in the parallel direction, as shown in Fig. 7, upon increasing the Li content from $LiC_{17.3}$ to $LiC_{5.8}$. Hence, we must conclude that this is the onset of the faster diffusion in the ordered regions that must be responsible for the selective increase of diffusion parallel to the fiber axis.

Yet, this explanation cannot *alone* account for the size of the difference between the diffusion coefficients in the two directions. Namely, with the *c* axis being dominantly *perpendicular* to the fiber axis (recall Fig. 6a), every ordered region exhibits fast Li diffusion *parallel* to the fiber axis. Perpendicular to the fiber axis, the *c* axis orientation is, by simplest assumption, isotropic. Relative to the magnetic field gradient that tests lithium diffusion perpendicular to the fiber axis the ordered domains can have two principal orientations: (i) their *c* axis oriented parallel and thereby their graphitic planes perpendicular that contributes to small average diffusion and (ii) their *c* axis oriented perpendicular and thereby their graphitic planes parallel that leads to fast diffusion. The orientation average of the effect[86] is shown as maximum $D_{\text{perpendicular}}/D_{\text{parallel}} = 2/\pi$ (see the ESI†) and this is clearly much larger than the experimental anisotropy that is 0.17 at 60% relative lithium content, as shown in Fig. 7. Hence, we must invoke some mesoscopic structure that selectively hinders diffusional displacement perpendicular to the fiber axis.

One possible large-scale hindrance could be constituted by voids or any other regions of the sample that are not permitted for Li. However, such hinderances would affect diffusion at both low and high Li contents which is not consistent with the data. Another intriguing possibility is that particular mesoscopic structures exist (that is, on the length scale they must be far below the diffusional pathlength $(4D\Delta)^{1/2}$ where factor-4 arises because of the 2D nature of the diffusion[88] perpendicular to the fiber axis and Δ is the diffusion time set to 10^{-1} s over the course of the experiments). Additional information can be obtained from the variation of the NMR spectrum with the direction of fiber axis with respect to the magnetic field, as shown in Fig. 8. Clearly, the quadrupole splitting exhibited by fibers oriented parallel to the magnetic field which show a rather peculiar behavior is *larger* than that for the perpendicular orientation!

The spectra shown in Fig. 8 are motionally averaged and thereby must reflect mesoscopic structure within the range of average diffusional displacement $(4D_{\text{perpendicular}}\tau)^{1/2}$. With τ as roughly 100 μs (see above) and $D_{\text{perpendicular}} \approx 10^{-12}$ m^2 s^{-1} (Fig. 7, at 60% Li content), the size of the relevant *diffusionally averaged domains* is set to about 20 nm. As shown in Fig. 8, these domains behave as if their local symmetry axis in eqn (2) is oriented *parallel* to the fiber axis. Yet, recall that XRD (*e.g.* Fig. 6a) clearly identifies that the *individual ordered domains that have an extension of a few nanometers* have their *c* axes dominantly perpendicular to the fiber axis. The only available

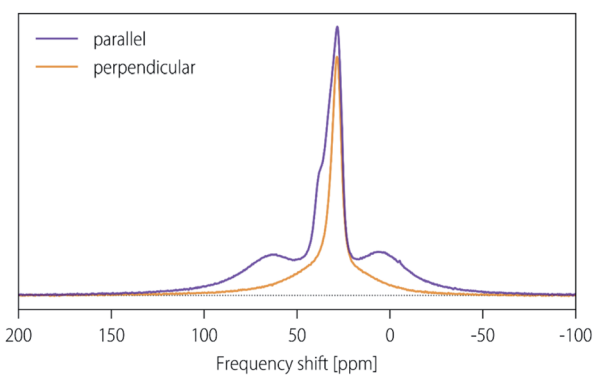

Fig. 8 The ^{7}Li NMR spectrum of the $LiC_{5.8}$ sample recorded with the fiber axis oriented parallel (as for all other figures) and perpendicular to the magnetic field at 343 K. The intensity was normalized for better visualization of satellites.

conclusion is that the ordered domains are not randomly distributed in the fiber but exhibit a mesoscopic structure where their joint arrangement is similar to that of being rolled up as is shown in the schematic in Fig. 7. In such a structure, Li diffusion along the roll axis would exhibit fast diffusion but a slow one perpendicular to the roll axis. The reason for this is the correlation among graphitic orientations. Namely, a large diffusional displacement along the graphitic planes would still not lead to a large *net* spatial displacement. Similar mesoscopic structures have indeed been identified by electron microscopy,[51,89] with the only difference that the mesoscopic structures we see are not "onion-like" (as inferred in these studies) but cylindrically rolled-up.

The PAN CF in this study has a pronounced preferential orientation uncommon in hard carbon. However, the asymmetric (002) analogue observed in the XRD pattern is entirely typical of such materials, albeit a little sharper than most.[10,90,91] It is therefore reasonable to presume that the division of the structure of PAN CFs into ordered and disordered regions which we described above is also typical of hard carbons. The oriented structure of PAN CFs presents a special case that allows NMR and 2D-XRD to be more precise than before. For example, the subtraction of the parallel XRD signal from the perpendicular signal, leaving only the structural information contained in the latter but not the former, is only possible in an oriented material recorded on a 2D detector. (One could perhaps create a pseudo-2D detector by rotating the sample and recording separate signals, but in most cases this will lack the surety that the exact same material has given rise to both patterns). The combination of NMR (which sensitively and selectively probes the Li environments) and XRD (probing the carbon structure *via* the (002) analogue) lends a great deal of credibility to the model, since they independently lead to the same interpretation of the electrochemical profile; there are two distinct kinds of carbon environments, both borrowing the layered structure of graphite; and that, at low specific capacities, lithium preferentially inserts into the kind that is disordered and only inserts into the ordered kind at higher specific capacitities. Our data do not explicitly reveal anything about how these ordered and disordered regions are related to each other; whether they are distinct phases or not, they clearly exist separately enough to give rise to different phenomena at the nanometer level. Combining the separation of ordered and disordered phases and previous research on the size[92] and curvature[11,93] of the graphene-like sheets, we present our proposed structural model of hard carbon shown in Fig. 9. The use of a 2D schematic sacrifices a degree of accuracy for a far larger degree of clarity. The ordered region (left) has a clear local orientation leading to multiple layers arranged in a broadly graphitic layered structure, but the curvature inevitably causes this to break down on a broader scale. The disordered region (right) lacks (most attributes of) three-dimensional local order. In addition, the disordered domains exhibit some spatial continuity since Li can diffuse over macroscopic distances within them – namely, at a low Li content the ^{7}Li signal attains no characteristic of the ordered sites (that is, it does not visit these sites) yet exhibits a diffusional displacement that is in the order of $(6D\Delta)^{1/2} \sim 10^{-6}$ m. Jointly, our data analysed in the framework of a rather simple model provide thereby a significant improvement concerning structural insight.

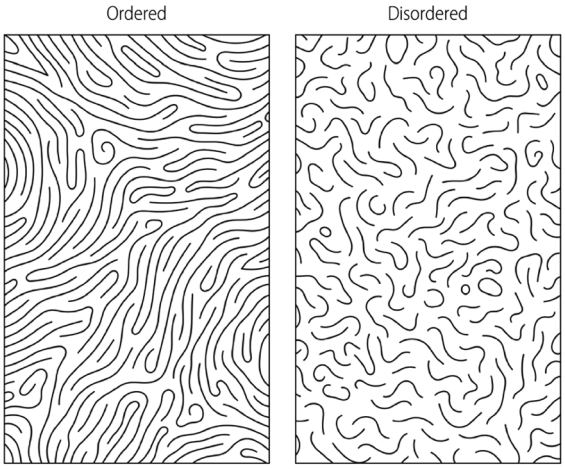

Fig. 9 A schematic of the structures of the ordered and disordered regions of hard carbon. In PAN CFs, these domains are intermingled on the <10 nm length scale, yet with spatial continuity for the disordered phase and mesoscopic orientation correlation for ordered domains as discussed in text.

Conclusions

Like any other heterogeneous material, hard carbons are inherently difficult to characterize. The difficulty lies with the large structural variation and with the limited ability of any experimental methods to capture this width. Hence, in hard carbons we know that there is some resemblance at the ordered end of the distribution to graphite (in terms of regularly arranged sheets of sp^2 hybridized carbon) and there is little resemblance to it at the other end. What is in-between can, of course, be pictured in models of various sophistications but seldom certified by experiments to a degree that makes one model more convincing than any other. With this observation at the outset, it is nevertheless the goal of this study to provide new insight into the structure of hard carbons centered on the application of these as the negative electrode in a battery – namely, what is the structure of Li insertion sites.

The difficulty with structural characterization outlined above calls for several methods to be applied. Good combinations are, supposedly, methods that have very different underlying principles and thereby very different sensitivities (and, thereby, bias) from structural details. The combination of ^{7}Li NMR spectroscopy, spin relaxation and diffusion with XRD fits that bill not only because of the distinct experimental principles but also because (i) the NMR observables report directly from the sites of insertion but only indirectly about the carbon matrix surrounding while (ii) the XRD observables report about the carbon matrix and how it is affected by Li.

The selected combination of methods is capable of providing meaningful structural information if one performs a careful joint analysis of the data. We attempted to do that here. In XRD, state-of-the-art correction and background suppression procedures were performed. In NMR, we put a lot of emphasis on the

motional averaging of the nuclear spin couplings, a feature that has often been neglected. This required temperature-dependent data and suitable dynamical information.

The structural information we obtained is rather consistent. First of all, the spectral features at the lowest explored temperatures reveal the large extent of the structural heterogeneity at the sub-nm-level. It is large and involves a few very small (∼nm) metallic particles. Upon increasing temperature, translational molecular motion averages spin couplings so that spectral features start to report about the order-disorder in regions at the several nm level. As also confirmed by XRD, at a low Li content Li is filled at sites with little graphitic character. Upon increasing the Li content, the ordered sites start to fill. Regarding either of these single points (heterogeneity and order/disorder), the information is not entirely novel but we claim that it is more encompassing and consistent.

The information regarding the mesoscopic order is novel. Here we detect ordered features which are best described as graphitic domains arranged in a vaguely cylindrical fashion coaxially along the fiber direction and their *c* axis oriented radially. Such features might have been detected by electron microscopy, though there were only cross-sectional images available and therefore the data were interpreted as "onion-like" structures.[51,89] Providing an in-depth understanding of Li storage in hard carbon, this work facilitates the development of a high-performance hard carbon negative electrode for LIBs and the combination of characterization can also be used to elucidate structural information of other carbonaceous materials.

Conflicts of interest

There are no conflicts to declare.

Acknowledgements

The authors acknowledge and thank Swedish Energy Agency for the support. Support from the Swedish Research Council (VR) is gratefully acknowledged. Parts of this research were funded by the Swedish Foundation for Strategic Research (SSF) within the Swedish national graduate school in neutron scattering (SwedNess). We acknowledge DESY (Hamburg, Germany), a member of the Helmholtz Association HGF, for the provision of experimental facilities. Parts of this research were carried out at PETRA III, and we would like to thank Andrei Chumakov and Stephan Roth for their assistance in using the P03 MINAXS beamline. Beamtime was allocated for proposal I-20190372.

References

1 M. Li, J. Lu, Z. Chen and K. Amine, *Adv. Mater.*, 2018, **30**, 1800561.
2 M. S. Whittingham, *Chem. Rev.*, 2004, **104**, 4271–4302.
3 K. Wang, Y. Xu, H. Wu, R. Yuan, M. Zong, Y. Li, V. Dravid, W. Ai and J. Wu, *Carbon*, 2021, **178**, 443–450.
4 L. Xie, C. Tang, Z. Bi, M. Song, Y. Fan, C. Yan, X. Li, F. Su, Q. Zhang and C. Chen, *Adv. Energy Mater.*, 2021, **11**, 2101650.
5 L. Zhao, Z. Hu, W. Lai, Y. Tao, J. Peng, Z. Miao, Y. Wang, S. Chou, H. Liu and S. Dou, *Adv. Energy Mater.*, 2021, **11**, 2002704.
6 D. Saurel, B. Orayech, B. Xiao, D. Carriazo, X. Li and T. Rojo, *Adv. Energy Mater.*, 2018, **8**, 1703268.
7 A. Kamiyama, K. Kubota, T. Nakano, S. Fujimura, S. Shiraishi, H. Tsukada and S. Komaba, *ACS Appl. Energy Mater.*, 2020, **3**, 135–140.
8 K. Sato, M. Noguchi, A. Demachi, N. Oki and M. Endo, *Science*, 1994, **264**, 556.
9 S. Alvin, H. S. Cahyadi, J. Hwang, W. Chang, S. K. Kwak and J. Kim, *Adv. Energy Mater.*, 2020, **10**, 2000283.
10 R. E. Franklin, *Proc. R. Soc. London, Ser. A*, 1951, **209**, 196–218.
11 A. Burian and J. Dore, *Acta Phys. Pol., A*, 2000, **98**, 457–468.
12 S. J. Townsend, T. J. Lenosky, D. A. Muller, C. S. Nichols and V. Elser, *Phys. Rev. Lett.*, 1992, **69**, 921–924.
13 P. J. F. Harris, *Philos. Mag.*, 2004, **84**, 3159–3167.
14 S. F. Parker, S. Imberti, S. K. Callear and P. W. Albers, *Chem. Phys.*, 2013, **427**, 44–48.
15 D. A. Stevens and J. R. Dahn, *J. Electrochem. Soc.*, 2000, **147**, 1271.
16 D. A. Stevens and J. R. Dahn, *J. Electrochem. Soc.*, 2001, **148**, A803.
17 M. Nagao, C. d. Pitteloud, T. Kamiyama, T. Otomo, K. Itoh, T. Fukunaga, K. Tatsumi and R. Kanno, *J. Electrochem. Soc.*, 2006, **153**, A914.
18 G. Yang, X. Li, Z. Guan, Y. Tong, B. Xu, X. Wang, Z. Wang and L. Chen, *Nano Lett.*, 2020, **20**, 3836–3843.
19 S. Huang, Z. Li, B. Wang, J. Zhang, Z. Peng, R. Qi, J. Wang and Y. Zhao, *Adv. Funct. Mater.*, 2018, **28**, 1706294.
20 S. Alvin, D. Yoon, C. Chandra, H. S. Cahyadi, J.-H. Park, W. Chang, K. Y. Chung and J. Kim, *Carbon*, 2019, **145**, 67–81.
21 Y. Yang, R. Fu and H. Huo, *NMR and MRI of Electrochemical Energy Storage Materials and Devices*, Royal Society of Chemistry, United Kingdom, 2021.
22 J. Conard and P. Lauginie, *TANSO*, 2000, **2000**, 62–70.
23 O. Pecher, J. Carretero-González, K. J. Griffith and C. P. Grey, *Chem. Mater.*, 2017, **29**, 213–242.
24 F. Blanc, M. Leskes and C. P. Grey, *Acc. Chem. Res.*, 2013, **46**, 1952–1963.
25 M. Mohammadi and A. Jerschow, *J. Magn. Reson.*, 2019, **308**, 106600.
26 K. Tatsumi, T. Akai, T. Imamura, K. Zaghib, N. Iwashita, S. Higuchi and Y. Sawada, *J. Electrochem. Soc.*, 1996, **143**, 1923–1930.
27 K. Tatsumi, J. Conard, M. Nakahara, S. Menu, P. Lauginie, Y. Sawada and Z. Ogumi, *J. Power Sources*, 1999, **81–82**, 397–400.
28 K. Zaghib, K. Tatsumi, Y. Sawada, S. Higuchi, H. Abe and T. Ohsaki, *J. Electrochem. Soc.*, 1999, **146**, 2784–2793.
29 S. Wang, H. Matsui, H. Tamamura, Y. Matsumura and T. Yamabe, *Phys. Rev. B: Condens. Matter Mater. Phys.*, 1998, **58**, 8163–8165.
30 Y. Sato, K. Tanuma, T. Takayama, K. Kobayakawa, T. Kawai and A. Yokoyama, *J. Power Sources*, 2001, **97–98**, 165–170.

31 S. E. Hayes, R. A. Guidotti, W. R. Even, P. J. Hughes and H. Eckert, *J. Phys. Chem. A*, 2003, **107**, 3866–3876.
32 K. Gotoh, M. Maeda, A. Nagai, A. Goto, M. Tansho, K. Hashi, T. Shimizu and H. Ishida, *J. Power Sources*, 2006, **162**, 1322–1328.
33 K. Guérin, M. Ménétrier, A. Février-Bouvier, S. Flandrois, B. Simon and P. Biensan, *Solid State Ionics*, 2000, **127**, 187–198.
34 S. Wong, R. A. Vaia, E. P. Giannelis and D. B. Zax, *Solid State Ionics*, 1996, **86–88**, 547–557.
35 N. Balke, S. Jesse, A. N. Morozovska, E. Eliseev, D. W. Chung, Y. Kim, L. Adamczyk, R. E. García, N. Dudney and S. V. Kalinin, *Nat. Nanotechnol.*, 2010, **5**, 749–754.
36 K. Persson, V. A. Sethuraman, L. J. Hardwick, Y. Hinuma, Y. S. Meng, A. van der Ven, V. Srinivasan, R. Kostecki and G. Ceder, *J. Phys. Chem. Lett.*, 2010, **1**, 1176–1180.
37 F. Yao, F. Güneş, H. Q. Ta, S. M. Lee, S. J. Chae, K. Y. Sheem, C. S. Cojocaru, S. S. Xie and Y. H. Lee, *J. Am. Chem. Soc.*, 2012, **134**, 8646–8654.
38 I. Umegaki, S. Kawauchi, H. Sawada, H. Nozaki, Y. Higuchi, K. Miwa, Y. Kondo, M. Månsson, M. Telling, F. C. Coomer, S. P. Cottrell, T. Sasaki, T. Kobayashi and J. Sugiyama, *Phys. Chem. Chem. Phys.*, 2017, **19**, 19058–19066.
39 M. H. Kjell, T. G. Zavalis, M. Behm and G. Lindbergh, *J. Electrochem. Soc.*, 2013, **160**, A1473–A1481.
40 M. A. Cabañero, N. Boaretto, M. Röder, J. Müller, J. Kallo and A. Latz, *J. Electrochem. Soc.*, 2018, **165**, A847–A855.
41 Y. Saito, H. Kataoka, K. Nakai, J. Suzuki, K. Sekine and T. Takamura, *J. Phys. Chem. B*, 2004, **108**, 4008–4012.
42 M. H. Kjell, E. Jacques, D. Zenkert, M. r. Behm and G. r. Lindbergh, *J. Electrochem. Soc.*, 2011, **158**, A1455.
43 N. Nitta, F. Wu, J. T. Lee and G. Yushin, *Mater. Today*, 2015, **18**, 252–264.
44 E. Jacques, M. Hellqvist Kjell, D. Zenkert, G. Lindbergh and M. Behm, *Carbon*, 2013, **59**, 246–254.
45 G. Fredi, S. Jeschke, A. Boulaoued, J. Wallenstein, M. Rashidi, F. Liu, R. Harnden, D. Zenkert, J. Hagberg, G. Lindbergh, P. Johansson, L. Stievano and L. E. Asp, *Multifunct. Mater.*, 2018, **1**, 015003.
46 S. J. Gibbs and C. S. Johnson, *J. Magn. Reson.*, 1991, **93**, 395–402.
47 S. L. Codd and P. T. Callaghan, *J. Magn. Reson.*, 1999, **137**, 358–372.
48 A. Buffet, A. Rothkirch, R. Dohrmann, V. Korstgens, M. M. Abul Kashem, J. Perlich, G. Herzog, M. Schwartzkopf, R. Gehrke, P. Muller-Buschbaum and S. V. Roth, *J. Synchrotron Radiat.*, 2012, **19**, 647–653.
49 G. Benecke, W. Wagermaier, C. Li, M. Schwartzkopf, G. Flucke, R. Hoerth, I. Zizak, M. Burghammer, E. Metwalli, P. Muller-Buschbaum, M. Trebbin, S. Forster, O. Paris, S. V. Roth and P. Fratzl, *J. Appl. Crystallogr.*, 2014, **47**, 1797–1803.
50 A. K. Soper and E. R. Barney, *J. Appl. Crystallogr.*, 2011, **44**, 714–726.
51 P. J. F. Harris and S. C. Tsang, *Philos. Mag. A*, 1997, **76**, 667–677.
52 A. P. Terzyk, S. Furmaniak, P. J. F. Harris, P. A. Gauden, J. Włoch, P. Kowalczyk and G. Rychlicki, *Phys. Chem. Chem. Phys.*, 2007, **9**, 5919–5927.
53 J. Hagberg, S. Leijonmarck and G. Lindbergh, *J. Electrochem. Soc.*, 2016, **163**, A1790–A1797.
54 E. Buiel and J. R. Dahn, *Electrochim. Acta*, 1999, **45**, 121–130.
55 H. Fujimoto, A. Mabuchi, K. Tokumitsu, N. Chinnasamy and T. Kasuh, *J. Power Sources*, 2011, **196**, 1365–1370.
56 M. J. Duer, *Introduction to Solid-State NMR Spectroscopy*, John Wiley and Sons Ltd, Oxford, UK, 2004.
57 I. Furó, *J. Mol. Liq.*, 2005, **117**, 117–137.
58 A. Abragam, *The Principles of Nuclear Magnetism*, Clarendon Press, Oxford, England, 1961.
59 K. Wang, Y. Xu, Y. Li, V. Dravid, J. Wu and Y. Huang, *J. Mater. Chem. A*, 2019, **7**, 3327–3335.
60 B. Halle and H. Wennerström, *J. Chem. Phys.*, 1981, **75**, 1928–1943.
61 C. A. Veracini, in *Nuclear Magnetic Resonance of Liquid Crystals*, ed. J. W. Emsley, Springer Netherlands, Dordrecht, 1985, p. 99.
62 R. Y. Dong, *Nuclear Magnetic Resonance of Liquid Crystals*, Springer, New York, 1997.
63 G. Roth, K. Lüders, P. Pfluger and H. J. Güntherodt, *Solid State Commun.*, 1981, **39**, 423–426.
64 K. Gotoh, T. Yamakami, I. Nishimura, H. Kometani, H. Ando, K. Hashi, T. Shimizu and H. Ishida, *J. Mater. Chem. A*, 2020, **8**, 14472–14481.
65 J. Langer, V. Epp, P. Heitjans, F. A. Mautner and M. Wilkening, *Phys. Rev. B: Condens. Matter Mater. Phys.*, 2013, **88**, 094304.
66 M. Vogel, O. Petrov, M. Trubitsyn, O. Nesterov and M. Volnianskii, *Ferroelectrics*, 2020, **558**, 46–58.
67 A. Kuhn, S. Narayanan, L. Spencer, G. Goward, V. Thangadurai and M. Wilkening, *Phys. Rev. B: Condens. Matter Mater. Phys.*, 2011, **83**, 094302.
68 K. Volgmann, V. Epp, J. Langer, B. Stanje, J. Heine, S. Nakhal, M. Lerch, M. Wilkening and P. Heitjans, *Z. Phys. Chem.*, 2017, **231**, 1215–1241.
69 W. Schmidt and M. Wilkening, *Solid State Ionics*, 2016, **287**, 77–82.
70 F. Kimmerle, G. Majer, U. Kaess, A. J. Maeland, M. S. Conradi and A. F. McDowell, *J. Alloys Compd.*, 1998, **264**, 63–70.
71 M. Trunnell, D. R. Torgeson, S. W. Martin and F. Borsa, *J. Non-Cryst. Solids*, 1992, **139**, 257–267.
72 K. Suzuki and S. Hayashi, *Solid State Ionics*, 2006, **177**, 3223–3231.
73 K. Volgmann, V. Werth, S. Nakhal, M. Lerch, T. Bredow and P. Heitjans, *Z. Phys. Chem.*, 2017, **231**, 1243–1262.
74 M. Mizuno, A. Hirai, H. Matsuzawa, K. Endo and M. Suhara, *Phys. Chem. Chem. Phys.*, 2001, **3**, 107–110.
75 F. Wright, *Phys. Rev.*, 1967, **163**, 420–431.
76 J. J. van der Klink and H. B. Brom, *Prog. Nucl. Magn. Reson. Spectrosc.*, 2000, **36**, 89–201.
77 R. Monot and J.-L. Millet, *J. Phys., Lett.*, 1976, **37**, 45–48.
78 C. Taupin, *J. Phys. Chem. Solids*, 1967, **28**, 41–47.
79 R. Kubo, A. Kawabata and S. Kobayashi, *Annu. Rev. Mater. Sci.*, 1984, **14**, 49–66.

80 C. P. Slichter, *Principles of Magnetic Resonance*, Springer, Berlin, Heidelberg, 1990.
81 J. Y. Howe, C. J. Rawn, L. E. Jones and H. Ow, *Powder Diffr.*, 2003, **18**, 150–154.
82 B. E. Warren, *Phys. Rev.*, 1941, **59**, 693–698.
83 B. E. Warren and P. Bodenstein, *Acta Crystallogr.*, 1965, **18**, 282–286.
84 H. Fujimoto and M. Shiraishi, *Carbon*, 2001, **39**, 1753–1761.
85 H. Jóhannesson, I. Furó and B. Halle, *Phys. Rev. E: Stat. Phys., Plasmas, Fluids, Relat. Interdiscip. Top.*, 1996, **53**, 4904–4917.
86 I. Furó and S. V. Dvinskikh, *Magn. Reson. Chem.*, 2002, **40**, S3–S14.
87 S. Matsuo and N. R. Sottos, *J. Appl. Phys.*, 2021, **130**, 115105.
88 W. S. Price, *NMR Studies of Translational Motion: Principles and Applications*, Cambridge University Press, Cambridge, 2009.
89 D. Ugarte, *Nature*, 1992, **359**, 707–709.
90 S. Ōtani, *Carbon*, 1965, **3**, 31–38.
91 T. Pfaff, F. M. Badaczewski, M. O. Loeh, A. Franz, J.-U. Hoffmann, M. Reehuis, W. G. Zeier and B. M. Smarsly, *J. Phys. Chem. C*, 2019, **123**, 20532–20546.
92 T. Ishii, S. Kashihara, Y. Hoshikawa, J.-i. Ozaki, N. Kannari, K. Takai, T. Enoki and T. Kyotani, *Carbon*, 2014, **80**, 135–145.
93 K. Jurkiewicz, M. Pawlyta, D. Zygadło, D. Chrobak, S. Duber, R. Wrzalik, A. Ratuszna and A. Burian, *J. Mater. Sci.*, 2018, **53**, 3509–3523.
94 C. Dong, H. Chen and F. Wu, *J. Appl. Crystallogr.*, 1999, **32**, 168–173.

